

# Global Collapses and Expansions in Star-Forming Clouds

Yang Gao<sup>1\*</sup> and Yu-Qing Lou<sup>1,2,3\*</sup>

<sup>1</sup>*Department of Physics and Tsinghua Centre for Astrophysics, Tsinghua University, Beijing 100084, China*

<sup>2</sup>*National Astronomical Observatories of China, Chinese Academy of Sciences, A20, Datun Road, Beijing 100012, China*

<sup>3</sup>*Department of Astronomy and Astrophysics, The University of Chicago, 5640 South Ellis Avenue, Chicago, IL 60637, USA*

Accepted 2009 August 29. Received 2009 August 28; in original form 2008 December 9

## ABSTRACT

Spectral molecular line profile observations of star-forming molecular clouds sometimes show distinct red asymmetric double-peaked molecular line profiles with weaker blue peaks and stronger red peaks. For some star-forming molecular clouds, such molecular transitions with red asymmetric line profiles and blue asymmetric line profiles (i.e. blue asymmetric double-peaked molecular line profiles with weaker red peaks and stronger blue peaks) may coexist in spatially resolved spectral observations, while for others, such molecular transitions with red asymmetric line profiles may completely dominate in spatially resolved spectral observations. Blue asymmetric line profiles are usually interpreted as signals of central core collapses, while red asymmetric line profiles remain unexplained. In this paper, we advance a spherically symmetric self-similar hydrodynamic model framework for envelope expansions with core collapses (EECC) of a general polytropic molecular gas cloud under self-gravity. Based on such EECC hydrodynamic cloud models, we perform tracer molecular line profile calculations using the publicly available RATRAN code for star-forming clouds with spectroscopic signatures of red asymmetric line profiles. The presence of red asymmetric line profiles from molecular cloud cores indicates that EECC processes are most likely an essential hydrodynamic process of star formation. With spatial distributions, we explore various profiles of molecular lines for several tracer molecules in different settings of EECC dynamic models with and without shocks.

**Key words:** hydrodynamics — ISM: clouds — line: profiles — radiative transfer — stars: formation — stars: winds, outflows

## 1 INTRODUCTION

Collapses, expansions, shocks and turbulence are several important dynamic features of star formation processes occurring inside molecular clouds. Such molecular cloud dynamic characteristics may be revealed by rich diagnostics and comprehensive analysis of molecular spectral emission line profiles. An extensively discussed theoretical framework of forming low-mass stars is the ‘inside-out collapse’ scenario (Shu 1977; Shu, Adams & Lizano 1987). This model describes an isothermal self-similar dynamic solution that has a collapsing core surrounded by a static envelope with an expanding boundary engulfing more and more mass into the collapsed region. By adopting empirically inferred temperature variations to replace the constant temperature, this dynamic collapse structure may lead to double-peak molecular line profiles with blue peaks stronger than red peaks (i.e. blue profiles), as revealed by spectral line

observations of some molecular globules in early stages of star formation (e.g. Zhou et al. 1993; Saito et al. 1999; Hogerheijde & Sandell 2000). Collapse solution based on dynamics of general polytropic gas sphere can also lead to blue profiles, yet with a temperature variation involved in the dynamic model in a self-consistent manner (Gao, Lou & Wu 2009).

Clearly, a collapse model is not a full story of star formation, as there exist observational signatures that cannot be accounted for in the collapse scenario (e.g. Wilner et al. 2000; Belloche et al. 2002; van der Tak, Caselli & Ceccarelli 2005). One important signature is the detected molecular emission lines with red asymmetry, i.e. optically thick emission lines are red shifted relative to optically thin lines from the same source. A statistical survey of the observed optically thick molecular lines show that a quarter up to  $\sim 30\%$  of all sources show red asymmetry (e.g. Mardones et al. 1997; Evans 2003; Fuller, Williams & Sridharan 2005). Among sources of red asymmetry, double-peak molecular line profiles with red peaks stronger than blue peaks (i.e. red profiles) are further identified (e.g. Park, Lee & Myers 2004;

\* E-mail: gaoyang-00@mails.tsinghua.edu.cn (YG); louyq@mail.tsinghua.edu.cn, lou@oddjob.uchicago.edu (Y-QL)

Tafalla et al. 2006; Velusamy et al. 2008). More specifically, for a number of known cloud sources, both red and blue asymmetries are observed towards the same transitions of the same molecules but at different beam offsets away from the centre (e.g. Tafalla et al. 1998; Matthews et al. 2006). While blue profiles are recognized as the signature of radial infalls or core collapses, what then do these red profiles imply?

Earlier radiative transfer calculations with parameterized flow structures indicate that rotation and radial outflows in molecular clouds may produce red profiles (e.g. Adelson & Leung 1988). Dynamics of bipolar outflows has been extensively studied in the past (e.g. Shu et al. 1991, 1994; Fiege & Henriksen 1996a; Ostriker 1997; Matzner & McKee 1999; Shang et al. 2006), and their spectroscopic signatures (e.g. molecular line profiles and radio maps) are also explored (e.g. Fiege & Henriksen 1996b). Being widely observed, these molecular bipolar outflows have velocities  $\gtrsim 10 \text{ km s}^{-1}$  (e.g. Wu et al. 2005; Su et al. 2007), which are too large to account for the widely observed red asymmetry signatures indicating a typical gas flow velocity of  $\sim 1 \text{ km s}^{-1}$  (e.g. Mardones et al. 1997; Fuller, Williams & Sridharan 2005). Of course, for special cases when bipolar outflows are oriented close to the plane of the sky, molecular line splittings can be smaller. Line profiles (as well as millimetre continuum maps) in a molecular cloud with bipolar outflow show an asymmetric spatial distribution according to the axis direction of the outflow (e.g. Di Francesco et al. 2001; Matthews et al. 2006; Jørgensen et al. 2007). Red profiles caused by rotation around the central core have a systematic displacement in the velocity of local standard of rest ( $V_{\text{LSR}}$ ) (Di Francesco et al. 2001, Redman et al. 2004). The spatial distribution of red profiles is also asymmetric according to the direction of the rotation axis (Park et al. 1992; Zhou 1995). Though generally considered to be part of contributions to the line broadening, turbulence in clouds is sometimes invoked to form line profiles with red or blue asymmetries, especially those more violent ones in the outer layers of clouds (e.g. Ossenkopf 2002; Lee & Kim 2009). Contraction and expansion motions caused by large-scale thermal pulsations (with a typical oscillation period of  $\sim 10^5 \text{ yr}$ ) in starless cores can also be origins of asymmetric molecular line profiles from molecular clouds in their early stages of star formation, i.e. starless cores (Lada et al. 2003; Redman, Keto & Rawlings 2006; Keto et al. 2006; Aguti et al. 2007).

Theoretical models of envelope expansion with core collapse (EECC) for star formation represent a significant recent development (Lou & Shen 2004; Shen & Lou 2004; Lou & Gao 2006; Wang & Lou 2008, Yu & Lou 2005; Yu et al. 2006; Hu & Lou 2008). Such EECC dynamic process might affect the initial mass function of stars (e.g. Nakano et al. 1995) and the environment of star formation (e.g. Matzner & McKee 2000; Moraghan, Smith & Rosen 2008). The crucial question is whether such global dynamic structures actually exist in star-forming clouds with sensible observational diagnostics such as characteristic features in molecular profiles? The main thrust of this paper is to show that theoretical molecular line profiles based on the general polytropic EECC solutions with collapses, expansions and shocks are able to explain observations of red profiles and

can further provide plausible inferences of the star-forming region.

This paper is structured as follows. We first present possible self-similar dynamic structures of collapse and expansion solutions for general polytropic molecular clouds (Wang & Lou 2008) in Section 2. Molecular spectral line profiles are then obtained from radiative transfer calculations in Section 3. Exploration of the EECC cloud conditions that generate red asymmetric line profiles and our perspective of model applications are also presented therein. We summarize and conclude in Section 4.

## 2 COLLAPSE AND EXPANSION DYNAMICS

### 2.1 General Polytropic Hydrodynamic Models

To describe star-forming molecular clouds, we adopt the general polytropic self-similar model framework of Wang & Lou (2008) but without the random magnetic field. In spherical polar coordinates  $(r, \theta, \phi)$ , nonlinear hydrodynamic partial differential equations (PDEs) for spherically symmetric molecular cloud dynamics are

$$\frac{\partial \rho}{\partial t} + \frac{1}{r^2} \frac{\partial}{\partial r} (r^2 \rho u) = 0, \quad (1)$$

$$\frac{\partial u}{\partial t} + u \frac{\partial u}{\partial r} = -\frac{1}{\rho} \frac{\partial p}{\partial r} - \frac{GM}{r^2}, \quad (2)$$

$$\frac{\partial M}{\partial t} + u \frac{\partial M}{\partial r} = 0, \quad \frac{\partial M}{\partial r} = 4\pi r^2 \rho, \quad (3)$$

$$\left( \frac{\partial}{\partial t} + u \frac{\partial}{\partial r} \right) \ln \left( \frac{p}{\rho^\gamma} \right) = 0, \quad (4)$$

where mass density  $\rho$ , radial flow velocity  $u$ , thermal gas pressure  $p$ , and enclosed mass  $M$  depend on radius  $r$  and time  $t$ ;  $G = 6.67 \times 10^{-8} \text{ dyne cm}^2 \text{ g}^{-2}$  is the gravitational constant and  $\gamma$  is the polytropic index. Equations (1) and (2) are mass and radial momentum conservations, respectively; equation (3) is another form of mass conservation. Equation (4) is the conservation of specific entropy along streamlines, which implies a general polytropic state equation (EoS)  $p = K(r, t)\rho^\gamma$  with  $K(r, t)$  being a coefficient that varies with both time  $t$  and radius  $r$  in general.

These nonlinear PDEs allow self-similar solutions and the pertinent self-similar transformation is given below

$$r = k^{1/2} t^n x, \quad (5)$$

$$u = k^{1/2} t^{n-1} v(x), \quad \rho = \frac{\alpha(x)}{4\pi G t^2}, \quad (6)$$

$$M = \frac{k^{3/2} t^{3n-2} m(x)}{(3n-2)G}, \quad p = \frac{kt^{2n-4} \alpha(x)^\gamma m(x)^q}{4\pi G}, \quad (7)$$

where  $x$  is the self-similar independent variable combining  $r$  and  $t$  in a special manner, and  $\alpha(x)$ ,  $m(x)$  and  $v(x)$  are dimensionless reduced mass density, enclosed mass and radial flow velocity, respectively. According to mass conservation equation (3), the reduced enclosed mass can be expressed as  $m(x) = \alpha(x)x^2[nx - v(x)]$ . Being an important thermodynamic variable, the gas temperature  $T$  is given by the ideal gas law

$$T \equiv \frac{p}{k_B \rho / (\mu m_H)} = \frac{\mu m_H}{k_B} k t^{2n-2} \alpha(x)^{\gamma-1} m(x)^q, \quad (8)$$

where  $k_B$ ,  $\mu$  and  $m_H$  are Boltzmann's constant, mean molecular weight and hydrogen mass, respectively. We shall adopt  $\mu \cong 1$  for typical star-forming clouds. For a finite  $dm(x)/dx$  as  $x \rightarrow 0$ , equation (7) gives a central mass accretion rate

$$\dot{M}_0 = k^{3/2} t^{3(n-1)} m_0 / G, \quad (9)$$

with  $m_0$  being the central reduced point mass enclosed. For  $n = 1$ , the central mass accretion rate  $\dot{M}_0$  remains constant; for  $n > 1$  and  $n < 1$ , this  $\dot{M}_0$  increases and decreases with increasing time, respectively. Indices  $\gamma$ ,  $n$  and  $q$  are related by general polytropic EoS (4) with  $q = 2(n+\gamma-2)/(3n-2)$ . The case  $n+\gamma = 2$  features an EoS for a conventional polytropic gas and  $\gamma = n = 1$  describes an isothermal gas. Self-similar transformation equations (5)–(7) make it possible to cast nonlinear PDEs (1)–(4) into nonlinear ordinary differential equations (ODEs) in terms of  $x$  which can be solved numerically with analytical asymptotic conditions and by taking care of the sonic critical curve (see Wang & Lou 2008 for details).

Analytically, we have a static equilibrium solution for spherical cloud, namely, a singular polytropic sphere (SPS)

$$v = 0, \quad \alpha = \left[ \frac{n^{2-q}}{2(2-n)(3n-2)} \right]^{-1/(n-3nq/2)} x^{-2/n},$$

$$m = n \left[ \frac{n^{2-q}}{2(2-n)(3n-2)} \right]^{-1/(n-3nq/2)} x^{(3n-2)/n} \quad (10)$$

(e.g. Lou & Hu 2009). This static SPS solution may be helpful for speculating the origin of those self-similar collapse and expansion solutions (see below).

In the limit of  $x \rightarrow +\infty$ , we have asymptotic similarity solution to the leading orders, viz.

$$\alpha = Ax^{-2/n},$$

$$v = \left[ -\frac{nA}{(3n-2)} + 2(2-n)n^{q-1}A^{1-n+3nq/2} \right] x^{(n-2)/n} + Bx^{(n-1)/n}, \quad (11)$$

where  $A$  and  $B$  are two constants of integration, referred to as the mass and velocity parameters, respectively. In the other limit of  $x \rightarrow 0^+$ , the asymptotic central free-fall solution is

$$v = -\left[ \frac{2m_0}{(3n-2)x} \right]^{1/2}, \quad \alpha = \left[ \frac{(3n-2)m_0}{2x^3} \right]^{1/2}, \quad (12)$$

where  $m = m_0$  is the reduced enclosed mass  $m(x) = \alpha x^2(nx - v)$  as  $x \rightarrow 0^+$  for a point mass at the very centre.

## 2.2 General Polytropic EECC Solutions

We mainly focus on self-similar dynamic solutions for envelope expansions with core collapse in the form of free-fall towards the cloud centre (i.e. EECC solutions; Lou & Shen 2004 and Shen & Lou 2004). Relevant parameters of five such selected self-similar solutions are listed in Table 1, where  $x_{\text{inf}}$  is the outgoing boundary separating the collapse and expansion regions;  $m_0$  is the dimensionless central reduced point mass; and  $m_{\text{tot}}$  is the total reduced enclosed mass of a spherical cloud with an expanding outer edge at  $x = 5$  for the star-forming cloud. We also list in Table 1 two important mass and velocity parameters  $A$  and  $B$ , which

characterize asymptotic dynamic behaviours for  $x \rightarrow +\infty$  and serve as asymptotic ‘boundary’ conditions in constructing general polytropic EECC solutions (see eqs (26) and (27) of Wang & Lou 2008 for details). Solutions IV and V are two EECC shock solutions with  $\gamma = 1.2$  and  $n = 0.8$ , the upstream point  $x_1$  and downstream point  $x_2$  correspond to the same shock radius  $R_{\text{sh}}$ ;  $v_1$  and  $v_2$  are the upstream and downstream reduced radial flow velocities, with negative value being infall and positive value being expansion, respectively.

Each of these selected EECC solutions has a central collapsed core and an outer expansion envelope with an outgoing interface at  $x_{\text{inf}}$  separating the two zones. At the beginning of evolution ( $t \rightarrow 0^+$ ), this boundary radius is approximately zero according to self-similar transformation (5), which indicates that collapse begins from the very centre of the cloud. As time goes on, this boundary radius increases with a constant  $x_{\text{inf}}$  at a variable speed of  $u_b = nk^{1/2}t^{n-1}x_{\text{inf}}$  according to equation (5), which means that more and more mass are enclosed into the collapse region (see expression (7)). At a given time  $t$ , mass densities and gas temperatures of all these EECC solutions increase towards the cloud centre. Shock solutions involve discontinuities of flow velocities, densities and temperatures across shock radius  $R_{\text{sh}}$ . Their dynamic structures are shown in Figs. 1 and 2 by adopting estimated physical scalings described below.

In constructing self-similar hydrodynamic solutions, we have presumed a priori the possible existence of such form of similarity solutions under plausible asymptotic conditions and actually derive them analytically and/or numerically from nonlinear hydrodynamic equations satisfying relevant physical constraints. Meanwhile, it is of considerable interest to figure out even qualitatively how a molecular cloud system can sensibly evolve into such a self-similar phase given a certain class of initial and boundary conditions. This is a challenge especially in view of the existence of several possible asymptotic self-similar solutions and requires a deeper theoretical understanding (e.g. Wang & Lou 2008). At this stage, we tentatively offer speculations on possible scenarios leading to self-similar EECC dynamic evolution invoked in this paper for modelling the dynamics of certain star-forming molecular clouds.

Similar to stellar oscillations widely studied observationally and theoretically, molecular clouds in SPS equilibrium (10) when somehow perturbed may give rise to acoustic pulsations on much larger spatial and temporal scales (e.g. Lada et al. 2003; Redman, Keto & Rawlings 2006; Keto et al. 2006; Aguti et al. 2007). For simplicity, we may envision purely radial acoustic pulsations with possible radial nodes in spherical molecular clouds; for example, such radial pulsations might be induced or excited by a sufficiently massive companion or transient object. With idealizations, such acoustic pulsations might persist periodically for a long time in molecular clouds. Realistically, such acoustic pulsations might be ‘damped’ in one or two ‘periods’ due to radiative losses as well as nonlinear effects. Among various pulsation phases, it would be possible to have a phase characterized by core contractions with envelope expansions. With such ‘initial’ conditions in molecular clouds, the nonlinear evolution may eventually lead to core collapse under the self-gravity while the envelope ex-

No.	$\gamma$	$n$	$q$	$x_{\text{inf}}$	$m_0$	$m_{\text{tot}}$	$A$	$B$	$x_1$	$v_1$	$x_2$	$v_2$
I	1.1	0.8	-1/2	1.50	1.49	5.0	3.5	2.2	—	—	—	—
II	1.2	0.8	0	1.77	2.32	10.0	5.0	2.4	—	—	—	—
III	1.2	0.9	2/7	1.80	3.74	20.8	10.0	2.4	—	—	—	—
IV	1.2	0.8	0	0.51	0.207	4.6	2.68	0.47	2.77	0.01	2.57	1.54
V	1.2	0.8	0	0.10	0.0254	9.2	7.72	3.70	1.70	-0.30	1.68	0.58

**Table 1.** Parameters of self-similar EECC dynamic solutions without and with shocks for five Models I–V labelled by roman numerals on the left most column. Among the three scaling indices  $\gamma$ ,  $n$  and  $q$ , only two are independent and all three are related by general polytropic EoS (4) with  $q = 2(n + \gamma - 2)/(3n - 2)$ . Three parameters  $x_{\text{inf}}$ ,  $m_0$  and  $m_{\text{tot}}$  are the dimensionless infall radius separating the inner collapse and outer expansion regions, the reduced central point mass, and the reduced total enclosed mass for a model cloud, respectively. Two coefficients  $A$  and  $B$  are mass and velocity parameters in asymptotic ‘boundary’ conditions in constructing corresponding self-similar solutions as  $x \rightarrow +\infty$ . Parameters  $x_1$ ,  $x_2$ ,  $v_1$  and  $v_2$  are the upstream and down stream locations and velocities for solutions across an outgoing shock front (i.e. Models IV and V).

pands into the surrounding interstellar medium (ISM). It is emphasized that no pulsations are necessarily persistent in this scenario. We speculate that this might evolve into self-similar EECC dynamic phase advanced in this paper. Following this scenario, pulsations of molecular clouds with different phases may evolve nonlinearly into a variety of dynamic states.

The EECC solution is necessarily consistent with the aspect of energy conservation. For most low-mass star formations, the Kelvin-Helmholz time scale  $t_{\text{KH}} = GM_{\text{tot}}^2/(RL)$  is longer than the dynamic timescale  $(\rho G)^{-1/2}$ , because of lower radiative efficiency (see e.g. McKee & Ostriker 2007). Here  $M_{\text{tot}}$ ,  $R$  and  $L$  are the total mass, the outer radius and the luminosity of the cloud, respectively. Because of radiative inefficiency, most low-mass star forming clouds need an extra means to carry out gravitational energy that are released during the central accretion. Global envelope expansion, which is a sensible dynamic solution as already shown, serves as the extra energy release. From the consideration of energy conservation, the EECC shock solutions may potentially offer valuable clues to the problem that accretion rates derived from observed luminosity are much smaller than those expected according to their dynamic evolution (i.e. the luminosity problem) in low-mass star formations (e.g. Kenyon et al. 1990; McKee & Ostriker 2007). For the physical scenario of variable central mass accretion rate and thus variable luminosity for the formation of low-mass stars in molecular clouds, we provide a general polytropic model explain the ‘luminosity problem’ (Lou & Dong 2009 in preparation).

### 2.3 Physical Properties of Molecular Clouds

The reduced dynamic variables should be converted to physical variables as applied to realistic cloud systems.

The typical infall radius of a molecular cloud is  $\sim 0.01 - 0.03$  pc (e.g. Myers 2005), or  $\sim 10^3 - 10^4$  AU. As the reduced infall radius is at  $x \sim 1$ , we may choose the length scale as  $k^{1/2} t^n \sim 4 \times 10^3$  AU

$$(13)$$

in self-similar transformation (5)–(7). The outer cloud radius is set at  $R \sim 2 \times 10^4$  AU. The number density at the infall radius is estimated by  $\sim 10^4 - 10^5$   $\text{cm}^{-3}$  (e.g. Harvey, Wilner & Myers 2003; Evans et al. 2009). A reduced number density of unity implies

$$(4\pi G \mu m_{\text{H}} t^2)^{-1} \cong 9 \times 10^4 \text{ cm}^{-3}, \quad (14)$$

leading to an estimated dynamic timescale. With parameter scalings (13) and (14) for clouds, physical variables of a cloud can be expressed as follows according to equations (5)–(9), namely

$$r = 4 \times 10^3 x \text{ AU}, \quad (15)$$

$$u = 0.213 v(x) \text{ km s}^{-1}, \quad (16)$$

$$N = 9 \times 10^4 \alpha(x) \text{ cm}^{-3}, \quad (17)$$

$$M = 0.204 m(x)/(3n - 2) M_{\odot}, \quad (18)$$

$$T = 5.33 \alpha(x)^{\gamma-1} m(x)^q \text{ K}, \quad (19)$$

$$\dot{M}_0 = 2.26 \times 10^{-6} m_0 M_{\odot} \text{ yr}^{-1}, \quad (20)$$

where  $N = \rho/(\mu m_{\text{H}})$  is the particle number density. We note that the dynamic timescale of a cloud is also automatically fixed, i.e.  $t_d \sim 2.2 \times 10^5$  yr according to scaling estimate (14). From scaling estimates (13) and (14), the sound parameter  $k$  is estimated by  $k^{1/2} = 3.76 \text{ km s}^{-0.9}$  for solution III and by  $k^{1/2} = 65.7 \text{ km s}^{-0.8}$  for solutions I, II, IV and V; while the upstream  $k^{1/2}$  jumps up to  $k^{1/2} = 70.8 \text{ km s}^{-0.8}$  and  $k^{1/2} = 66.5 \text{ km s}^{-0.8}$  on the downstream side of shock solutions IV and V, respectively.

With scaling expressions (13) and (14), we estimate physical properties of star-forming clouds as exemplified by Models I through V tabulated in Table 2. Figures 1 and 2 illustrate the radial profiles for physical variables of these model clouds in two sets.

For those Models without shocks (i.e. I, II and III), the infall radius  $R_{\text{inf}}$  are similar to each other, and their central core mass  $M_0$  and total mass  $M_{\text{tot}}$  are also comparable. Here, the infall radius  $R_{\text{inf}}$  may be fairly small at the onset of a cloud core collapse and expands to encompass more gas and dust particles into the collapsed region as time goes on. We note in Fig. 1 that the overall number density and temperature values increase from Model I to III; and the temperature of Model III increases slightly outwards at large radii ( $\sim 10^4$  AU). We note in Table 2 a gradual increase of the two masses  $M_0$  and  $M_{\text{tot}}$  from Model I to Model III, caused by the increasing mass parameter  $A$  as shown in Table 1 [see equation (26) in (Wang & Lou 2008)]. Our numerical explorations reveal that as  $n + \gamma$  increases, the presence of EECC solutions calls for increasing values of  $A$ . Another variation is that the ratio of central mass point to the total

No.	$\gamma$	$n$	$M_0$	$M_{\text{tot}}$	$\dot{M}_0$ ( $M_\odot \text{ yr}^{-1}$ )	$R_{\text{inf}}$ (AU)	$R_{\text{sh}}$ (AU)	$u_1$	$u_2$
I	1.1	0.8	$0.75 M_\odot$	$2.52 M_\odot$	$3.38 \times 10^{-6}$	$6.0 \times 10^3$	—	—	—
II	1.2	0.8	$1.18 M_\odot$	$5.10 M_\odot$	$5.30 \times 10^{-6}$	$7.1 \times 10^3$	—	—	—
III	1.2	0.9	$1.91 M_\odot$	$11.00 M_\odot$	$8.41 \times 10^{-6}$	$7.2 \times 10^3$	—	—	—
IV	1.2	0.8	$0.106 M_\odot$	$2.34 M_\odot$	$4.73 \times 10^{-7}$	$2.04 \times 10^3$	$11.1 \times 10^3$	$0.002 \text{ km s}^{-1}$	$0.34 \text{ km s}^{-1}$
V	1.2	0.8	$0.012 M_\odot$	$4.68 M_\odot$	$5.77 \times 10^{-8}$	$0.40 \times 10^3$	$6.8 \times 10^3$	$-0.07 \text{ km s}^{-1}$	$0.13 \text{ km s}^{-1}$

**Table 2.** Physical parameters of cloud Models I–V, with  $\gamma$  and  $n$  being their polytropic indices and scaling indices, respectively. Two dimensional masses  $M_0$  and  $M_{\text{tot}}$  are the central point mass and the total cloud mass inside  $R = 2 \times 10^4$  AU, while  $\dot{M}_0$  denotes the central mass accretion rate. Being the infall radius,  $R_{\text{inf}}$  is the boundary between the infall and outflow regions. Parameter  $R_{\text{sh}}$  is the outgoing shock radius for shock solutions in Models IV and V, and  $u_1$  and  $u_2$  are the upstream and downstream radial flow velocities, with negative values denoting inflows.

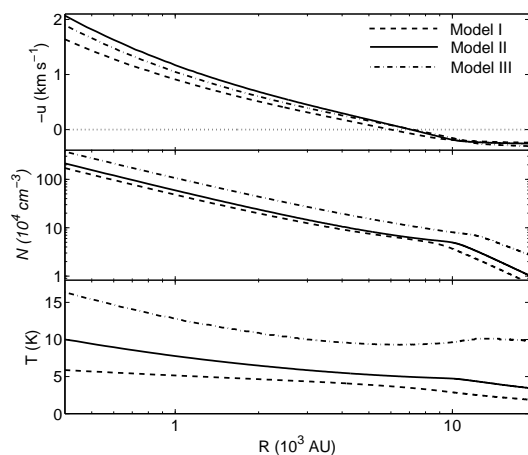


**Figure 1.** Radial profiles for physical variables of three EECC dynamic models I, II and III, with different polytropic indices  $\gamma$  and  $n$  yet without shocks. From top to bottom are: radial flow velocity (positive values for infall), number density and temperature profiles. The abscissa is radius  $R$  in  $10^3$  AU in a logarithmic scale. Dashed, solid and dash-dotted curves are the EECC dynamic solutions for Model I with  $\gamma = 1.1$  and  $n = 0.8$ , Model II with  $\gamma = 1.2$  and  $n = 0.8$ , and Model III with  $\gamma = 1.2$  and  $n = 0.9$ , respectively. The dotted horizontal line in the top panel is for the zero velocity line  $u = 0 \text{ km s}^{-1}$ . The infall radii for Models I, II and III are  $R_{\text{inf}} = 6.0 \times 10^3$  AU,  $R_{\text{inf}} = 7.1 \times 10^3$  AU and  $R_{\text{inf}} = 7.2 \times 10^3$  AU, respectively. Other parameters for these general polytropic self-similar solutions are summarized in Tables 1 and 2.

mass  $M_0/M_{\text{tot}}$  decreases from  $\sim 29.9\%$  of Model I to  $\sim 23.2\%$  of Model II to  $\sim 17.4\%$  of Model III. This phenomena may be explained by accounting for general polytropic SPS solution (10), of which smaller  $\gamma$  and  $n$  values lead to mass distributions with more central concentration.

By comparing Models II, IV and V, we can infer the effects of shocks in self-similar EECC dynamic solutions. From Fig. 2, we see that central infall velocities for EECC solutions with shocks (i.e. Models IV and V) are greatly suppressed, and their infall radii  $R_{\text{inf}}$  are smaller as compared to Model II without shock (Table 2). As a consequence, the central mass accretion rate  $\dot{M}_0$  and the central mass  $M_0$  for Models IV and V are smaller, taking only 10% and 1% the values of Model II, respectively. The low values of mass accretion rates and central masses make these shock solutions potentially applicable for the formation of brown dwarfs. We should also note from Table 2 that the total mass  $M_{\text{tot}}$  for

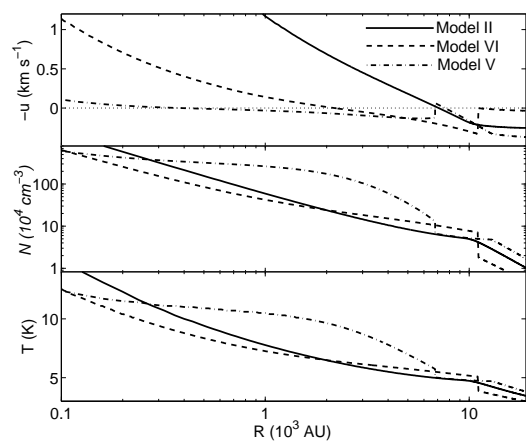


**Figure 2.** Radial profiles for physical variables of three EECC dynamic Models II, IV and V, with and without shocks for polytropic index  $\gamma = 1.2$  and scaling index  $n = 0.8$ . From top to bottom are: radial flow velocity (positive values for infall), number density and temperature profiles. The abscissa is radius  $R$  in  $10^3$  AU in a logarithmic scale. Solid, dashed and dash-dotted curves are the solutions for Model II without a shock, Model IV with a shock at  $R_{\text{sh}} = 11.1 \times 10^3$  AU, and Model V with a shock at  $R_{\text{sh}} = 6.8 \times 10^3$  AU, respectively. The horizontal dotted line in the top panel is for the zero velocity line  $u = 0 \text{ km s}^{-1}$ . The infall radii for Models II, IV and V are  $R_{\text{inf}} = 7.1 \times 10^3$  AU,  $R_{\text{inf}} = 2.04 \times 10^3$  AU and  $R_{\text{inf}} = 0.40 \times 10^3$  AU, respectively. Other parameters for these self-similar EECC solutions are summarized in Tables 1 and 2.

these three models are comparable, which suggests the possibility that under certain conditions protostars with different masses may form from molecular clouds with similar masses. In other words, molecular clouds of comparable masses have additional freedoms to give rise to central protostars of different masses. The very low masses and mass accretion rates of EECC shock solutions are caused by efficient envelope expansions with small inner boundary radius (Table 2). Inside the shock radius  $R_{\text{sh}}$ , the particle number density  $N$  and gas temperature  $T$  of Models IV and V are higher than or close to those of Model II (see Figure 2).

From Table 2, we get the information that the central mass of a cloud (i.e. protostellar mass) is not tightly or directly related to the total cloud mass for different model solutions, especially for EECC dynamic solutions with shocks. This conclusion agrees with the result that the star forming efficiency  $M_0/M_{\text{tot}}$  is mainly

determined by the comparison between mass accretion and outflow rates (e.g. bipolar outflows therein), and is weakly dependent on the core mass<sup>1</sup>  $M_{\text{tot}}$  and number density  $N$  (e.g. Nakano, Hasegawa & Norman 1995; Matzner & McKee 2000). However, a constant ratio between mass outflow and accretion rates is always presumed for a certain multi-star-forming cloud, and the conclusion that initial mass function (IMF) of protostars should be closely connected with the cloud mass function (CMF) is usually drawn (e.g. Hennebelle & Chabrier 2008; Myers 2008). But there is no obvious reason that protostars forming in the same cloud should have the same mass outflow ratio over accretion. Based on our analysis and results, we strongly suggest that solutions with different ratios between outflow and accretion exist in the same molecular cloud, and IMF of protostars can differ from CMF significantly, especially for those protostars with extremely low masses (i.e. brown dwarfs).

### 3 SPECTRAL LINE PROFILE SIGNATURES

We perform radiative transfer calculations for molecular spectral line profiles using the publicly available numerical code RATRAN (Hogerheijde & Sandell 2000) under spherical symmetry. This RATRAN code has been benchmarked among seven other radiative transfer codes by Van Zadelhoff et al. (2002) against examples of star forming clouds like B335. Based on the Monte Carlo method (e.g. Hammersley & Handscomb 1964; Shreider 1966; Bernes 1979), this RATRAN code deals with both radiative transfer and non-local thermal equilibrium (non-LTE) excitations of atomic and molecular lines, making it readily adaptable to realistic astrophysical cloud systems.<sup>2</sup> We adopt dynamic cloud models for line profile calculations. The dynamic and thermal parameters, namely radial flow velocity  $u$ , number density  $N$  and gas kinetic temperature  $T$  are obtained consistently from the general polytropic EECC dynamic Models I–V. The temperature of dusts in a cloud is assumed to follow the gas kinetic temperature  $T$ . From the cloud centre to its outer radius  $R = 20000$  AU, a molecular cloud is divided into 12 shells with enough accuracy for calculations (8 and 10 shells are also tested separately but with little variance in line profiles). However, physical properties of these shells are not uniform in order to show the transition between infall and outflow for all the dynamic models.

In Figs. 3, 4 and 5, we show a sample of computed molecular line profiles, viz.  $\text{HCO}^+$   $J=1-0$  at 89.19 GHz and  $\text{HCO}^+$   $J=3-2$  at 267.56 GHz, for the five dynamic EECC solution Models I–V. Molecular line profiles for transitions CO  $J=2-1$  at 230.54 GHz,  $\text{C}^{18}\text{O}$   $J=1-0$  at 109.78 GHz, CS  $J=2-1$  at 97.98 GHz and  $\text{N}_2\text{H}^+$   $J=1-0$  at 93.13 GHz are shown in Figs. 6 and 7. All molecular data are obtained from the Leiden Atomic and Molecular

Database (Schöier et al. 2005). Emission line profiles with different impact parameters  $b$  [i.e. distance of line of sight (LOS) from the cloud centre] and under different conditions of micro turbulence are shown in these figures. More compressed separations between impact parameters for pointings are chosen for LOS passing through the most inner regions of clouds, in order to clearly show the transitions between blue profiles and red profiles for Models I–III. The number density of  $\text{HCO}^+$  molecules is assumed to be proportional to the overall molecular number density with a constant ratio, i.e.  $N_{\text{HCO}^+} = 2 \times 10^{-9}N$ . Molecules in Figs. 6 and 7 are also assumed to be of constant abundance ratios, viz.  $N_{\text{CO}} = 5 \times 10^{-5}N$ ,  $N_{\text{C}^{18}\text{O}} = 1 \times 10^{-7}N$ ,  $N_{\text{CS}} = 3 \times 10^{-9}N$  and  $N_{\text{N}_2\text{H}^+} = 1.5 \times 10^{-10}N$ , respectively. All these molecular abundances are chosen according to Tafalla et al. (2006), and the central abundance hole derived from fitting procedure therein is not assumed in our model calculations. Strictly speaking, for all molecules, the variation of abundance ratio should be seriously taken into account (Rawlings & Yates 2001; Tsamis et al. 2008), and the constant ratio abundance adopted here is just a first order approximation.

#### 3.1 Red Profiles from EECC Dynamic Models

The most distinct spectroscopic signature of EECC dynamic models with core collapses and envelope expansions is the double-peak molecular line profile with the red peak being stronger than the blue peak, referred to as the red profile. We readily see such red profiles from cloud models described by each EECC solution in Figs. 3–5. A more generic type of red profiles has no obvious central dip but shows a stronger red shoulder, which exist over a larger range of impact parameter  $b$  for the LOS. In Figs. 6 and 7, red profiles also widely exist except for CO and  $\text{C}^{18}\text{O}$  transitions in Model III (Fig. 6).

We demonstrate two types of self-similar EECC dynamic solutions according to the appearance of red profiles for molecular spectral lines from star-forming clouds. For Models I, II and III, red profiles only exist for a fairly large impact parameter  $b$ , i.e. in Fig. 3,  $b \gtrsim 1.08 \times 10^3$  AU for Models I and III, and  $b \gtrsim 1.35 \times 10^3$  AU for Model II; while inside these radii (i.e. impact parameter), blue profiles for molecular lines emerge because of the more dominant role of core collapse towards the centre. This type of spatial transitions from blue profiles to red profiles can be seen in some molecular clouds with spatially resolved observations (e.g. Tafalla et al. 2000; Ward-Thompson & Buckley 2001), although not sufficiently spherically symmetric. For Models IV and V, whose infall radii are very small at the chosen epochs, red profiles for molecular lines exist throughout pixels with a range of impact parameter  $b$ ; this can also be seen in some of recent observations (Thompson & White 2004; Aguti et al. 2007). These results of our numerical exploration clearly indicate that the broad existence of red profiles is a characteristic signature of global envelope expansion, in contrast to the blue profiles which are characteristic feature of core collapse (e.g. Zhou et al. 1993; Gao, Lou & Wu 2009). For all these EECC dynamic models without or with shocks, molecular emission line profiles decrease in the overall magnitudes as the LOS departs away from the core centre and gradu-

<sup>1</sup> We use the two terms ‘core mass’ and ‘cloud mass’ interchangeably in the loose sense.

<sup>2</sup> For the purpose of testing and checking, our simple model radiative transfer calculations (Gao, Lou & Wu 2009) are also performed by adjusting optical depths in parallel to the RATRAN code calculations for samples of red profiles. The relevant results are comparable.

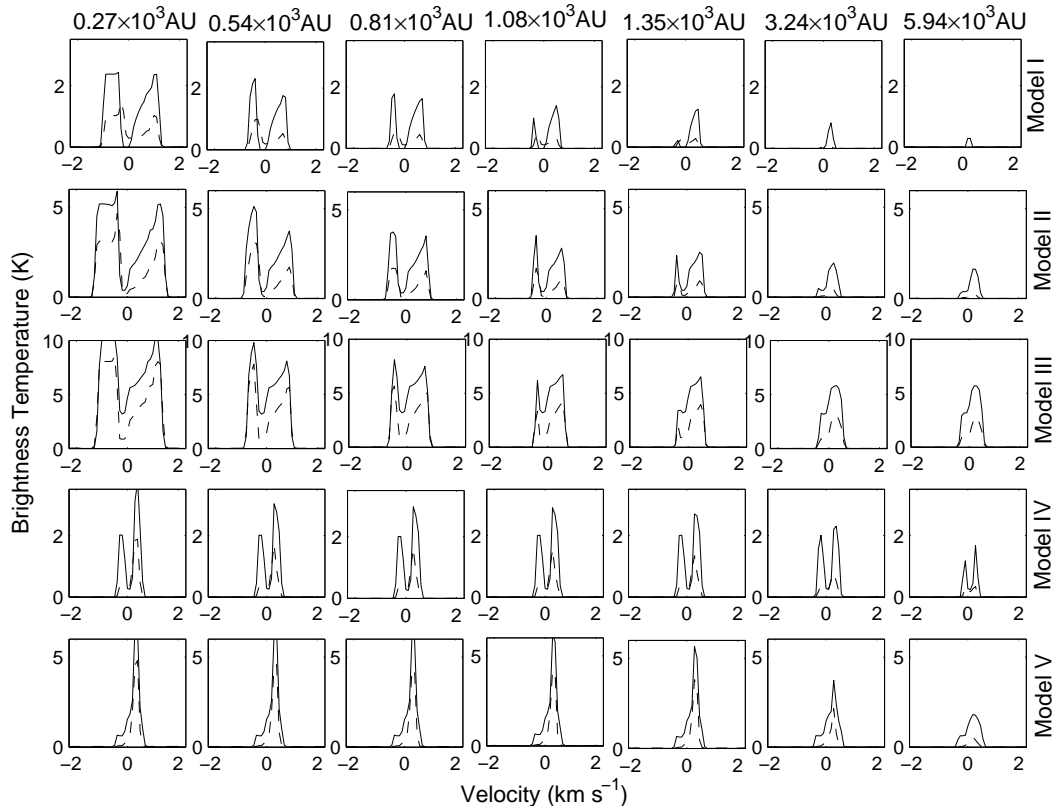


**Figure 3.** Computed molecular line profiles of  $\text{HCO}^+(1-0)$  at 89.19 GHz (solid curves) and  $\text{HCO}^+(3-2)$  at 267.56 GHz (dashed curves) from individual pixels of spatially resolved emission lines for five EECC dynamic models, viz. Models I–V. The ordinate is the brightness temperature in Kelvin and the abscissa is the projected velocity component along the LOS in the local standard of rest (LSR) in unit of  $\text{km s}^{-1}$ . Rows from top to bottom show molecular line profiles for different dynamic Models I–V, respectively. Panels from left to right present LOS with seven different impact parameter  $b$  (i.e.  $0.27 \times 10^3$  AU,  $0.54 \times 10^3$  AU,  $0.81 \times 10^3$  AU,  $1.08 \times 10^3$  AU,  $1.35 \times 10^3$  AU,  $3.24 \times 10^3$  AU,  $5.94 \times 10^3$  AU). Impact parameters for pointings are not uniformly chosen on purpose such that the transitions between blue profiles and red profiles can be clearly identified for Models I, II and III; meanwhile, the spatial coverage is sufficiently large to show variations of molecular line profiles. Containing both turbulence and thermal effects, the intrinsic line broadening is chosen as  $\Delta u = 0.17 \text{ km s}^{-1}$ .

ally disappear as cloud density and temperature decrease further.

By comparing molecular line profiles among Models I, II and III, we find slight differences caused by different EECC dynamic profiles. The higher spectral amplitude in Model III appears to be caused by the higher number density and gas kinetic temperature involved (Fig. 1). The central dips for line profiles of Model III are shallower than those from Models I and II; this is probably because of the gradual temperature rise at outer radii of Model III (Fig. 1). However, we cannot immediately claim that these differences in molecular line profiles are caused by different values of polytropic index  $\gamma$  and scaling index  $n$  in dynamic models, as for the same set of indices, different asymptotic boundary conditions will also lead to considerable variations in dynamic profiles (see e.g. Lou & Gao 2006; Wang & Lou 2008; Hu & Lou 2008). For Models IV and V, molecular emission lines with red profiles present for all values of impact parameter  $b$ . Then how could we understand the role of expanding shocks in these self-similar EECC dynamic solutions? Dynamically, in gas clouds with relatively smooth or less dras-

tic mass density profile, shocks are more likely to happen, which push more mass outwards and lead to more effective envelope expansions. The broad existence of red profiles just represents small infall radius at the epoch and highly efficient envelope expansion. Therefore by referring to underlying dynamic models, the presence of red profiles for nearly all impact parameter  $b$  indicates that the central protostellar mass is very small (i.e.  $\sim 0.106 M_{\odot}$  in Model IV and  $\sim 0.012 M_{\odot}$  in Model V) and the molecular cloud may form a brown dwarf at the centre.

### 3.2 Effects of Optical Depth and Turbulence

Proper optically thick conditions (i.e. absorption and scattering) in star-forming molecular clouds are responsible for such asymmetric spectroscopic signatures as in Figs. 3–5. Both  $\text{HCO}^+ J=1-0$  and  $J=3-2$  transitions are deeply self-absorbed (e.g. Tafalla et al. 2006), while the  $J=3-2$  line transition has a lower optical depth and source function because of lower level populations on  $J=3$  and  $J=2$  at such a cold environment with  $T \sim 10$  K. This contrast causes

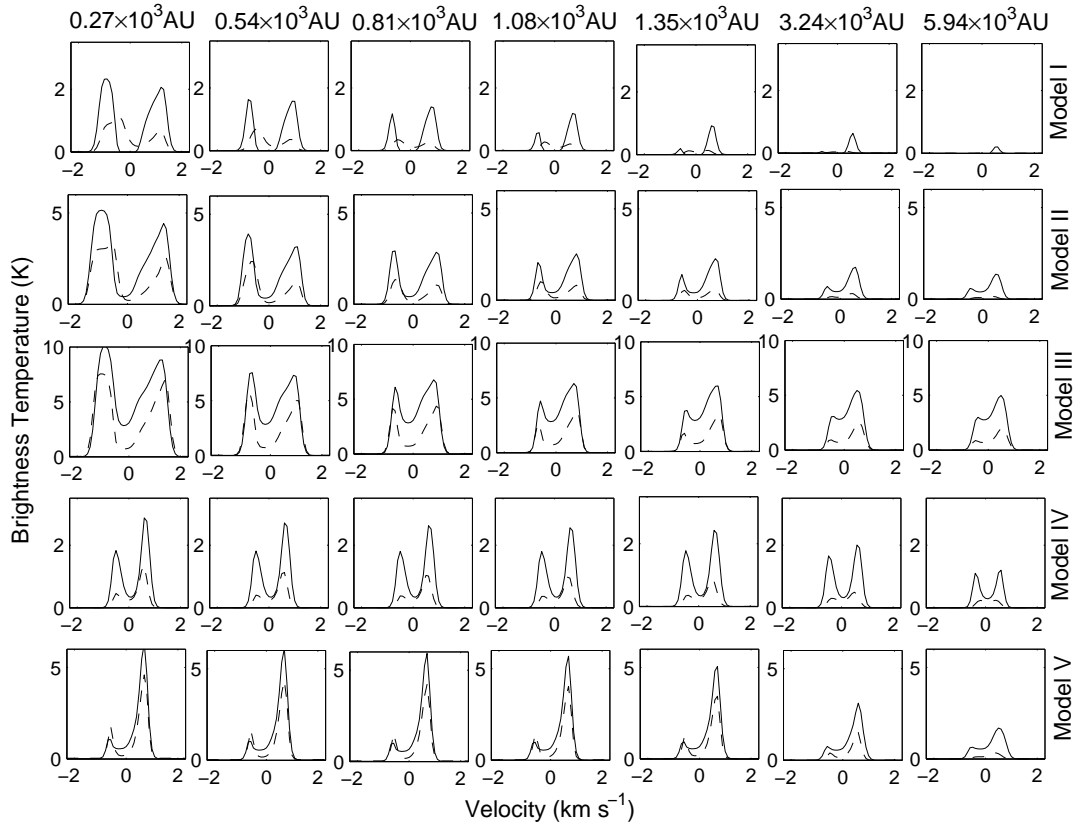


**Figure 4.** Similar RATRAN computations for molecular spectra line profiles for five EECC dynamic Models I–V as in Fig. 3, but with intrinsic line broadening  $\Delta u = 0.5 \text{ km s}^{-1}$ . This intrinsic line broadening contains both turbulence and thermal effects.

two effects on molecular line profiles: first, the intensities of  $J=3-2$  lines are weaker; and secondly, asymmetries of molecular line profiles are less apparent for  $J=3-2$  transitions. This comes to a widely tested conclusion that optically thick transition lines offer diagnosis for the large-scale thermal and dynamic structures of molecular clouds. CO and CS transitions in Figs. 6 and 7 are also examples of optically thick transitions, which show distinct red profiles. In contrast,  $\text{C}^{18}\text{O}$  and  $\text{N}_2\text{H}^+$  transitions are examples of optically thin transitions, which simply show single peak line profiles.

Turbulence in molecular clouds is another important aspect that affects molecular line profiles in a significant manner (e.g. Arons & Max 1975; Larson 1981; Lou & Rosner 1986; Zweibel & McKee 1995; MacLow 1999). In this paper, the effect of turbulence is subsumed in the form of the intrinsic line broadening  $\Delta u$ , where another contribution to the broadening is thermal broadening of  $\Delta u_{\text{the}} \sim 0.1 \text{ km s}^{-1}$  for clouds with a temperature of  $\sim 10 \text{ K}$ . We show radiative transfer results for a smaller or comparable turbulent broadening in Figs. 3 and 4, and molecular line profiles for clouds under stronger turbulence are shown in Fig. 5. Besides the increase of line width, line profile asymmetry decreases as a result of the enhanced turbulence.

### 3.3 Star-Forming Molecular Clouds

By fitting spatially resolved spectral line profiles to real molecular clouds, we may infer their underlying dynamic structures, and further estimate physical parameters (e.g. protostellar mass, central mass accretion rate, dynamic age etc.) of star-forming molecular cloud cores. There are several aspects for the data fitting: (1) selection of self-similar EECC dynamic solutions, (2) adoption of proper physical scalings derived from empirical information and (3) choice of suitable turbulent broadening. Additionally, sub-millimeter continuum observations can serve as a constraint on the radial profiles of density and temperature (e.g. Adams 1991; Shirley et al. 2000; Harvey, Wilner & Myers 2003) before fitting to molecular spectral emission line profiles. For describing more realistic cloud situations, variations of molecular abundance ratio should be taken into account. Star-forming molecular clouds L1517B (e.g. Tafalla et al. 2006), L1544 (e.g. van der Tak, Caselli & Ceccarelli 2005), L1551NE (e.g. Moriarty-Schieven, Butner & Wannier 1995), L483 (e.g. Park et al. 2000; Tafalla et al. 2000, Carolan et al. 2008) are among the good candidates of molecular clouds likely involving EECC dynamic motions.

In addition to red profiles for molecular lines, there are several other clues when applying EECC dynamic models to molecular clouds. Global cloud systems have an estimated



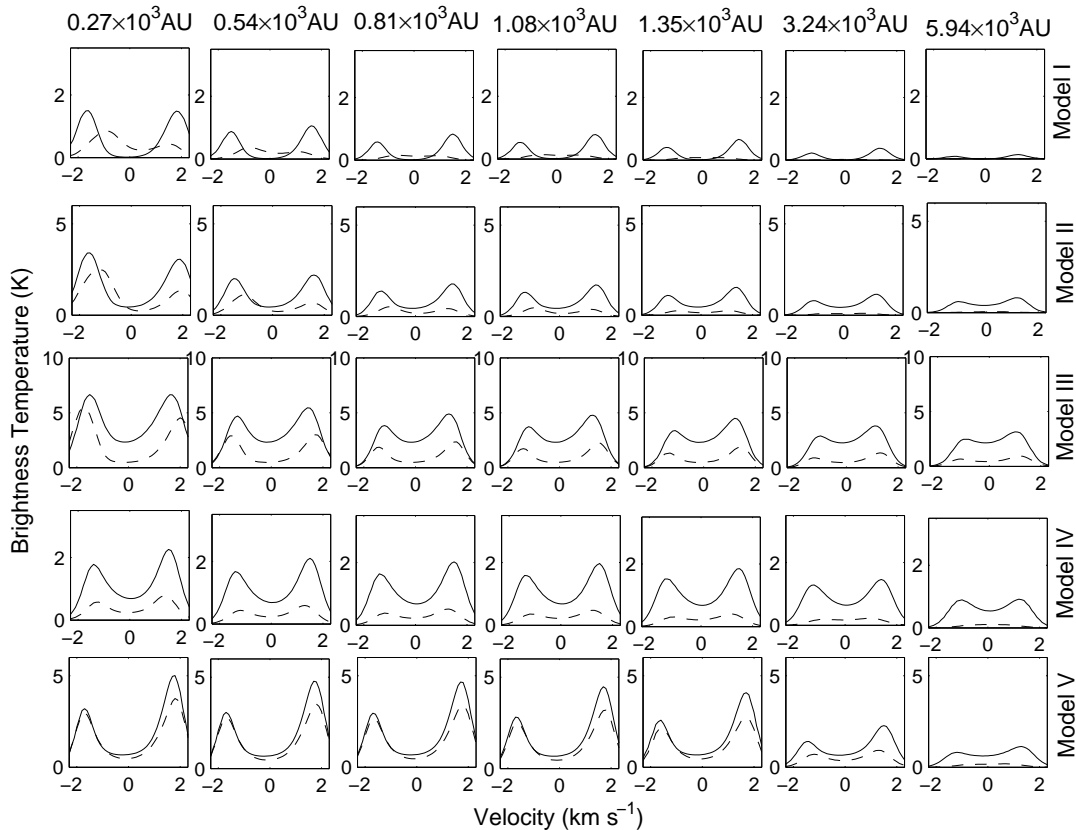


**Figure 5.** Similar RATRAN computations for molecular spectral line profiles for five EECC dynamic Models I–V as in Fig. 3, but with intrinsic line broadening  $\Delta u = 1.5 \text{ km s}^{-1}$ . This intrinsic line broadening contains both turbulence and thermal effects.

speed range of  $\sim 0.1 - 1 \text{ km s}^{-1}$  for flows, which is smaller than bipolar outflows of typical speed  $\gtrsim 10 \text{ km s}^{-1}$ . Observed with sufficient spatial resolutions, molecular line profiles from clouds with EECC dynamics will manifest a circular symmetry; while bipolar outflows have line emissions with a bipolar asymmetry in spatial distributions, as we mentioned in Section 1. Frequency resolution of about  $0.1 \text{ km s}^{-1}$  is needed to resolve spectroscopic signatures as shown in Figs. 3 to 5. High spatial resolution (e.g.  $2''$  or smaller for molecular clouds at  $\sim 200 \text{ pc}$ ) is also very important for detecting variations of molecular line profiles as a function of radius in cloud core, which helps to distinguish different underlying dynamic structures.

#### 4 SUMMARY AND CONCLUSIONS

We invoke self-similar general polytropic EECC dynamic solutions without or with shocks to model the global evolution of a certain class of molecular clouds. By specifying relevant parameters plausibly estimated for molecular clouds, we illustrate several examples of general polytropic EECC cloud solutions. On the basis of these cloud solutions, we perform radiative transfer calculations to produce molecular line profiles to confirm the viability of EECC model framework.

Through extensive numerical explorations, we demonstrate that the widely observed ‘red profiles’ in molecular

emission spectral lines from star-forming clouds may well serve as important diagnostics for revealing the underlying EECC self-similar hydrodynamics in molecular clouds (Lou & Shen 2004; Shen & Lou 2004; Lou & Gao 2006; Wang & Lou 2008). From the point of view of general polytropic hydrodynamics and radiative transfer, our explanation for the mystery of ‘red profiles’ in emission spectral lines appears natural and physically sensible. In particular, a molecular cloud characterized by an envelope expansion with a simultaneous central core collapse represents novel scenario. Based on EECC solutions with or without shocks, optically thick molecular emission lines from gas clouds can show red profiles for all impact parameter  $b$  of LOS from the cloud centres, or just outside a certain  $b$  value (with the inner region showing blue profiles). The optical depth of transition lines and turbulent broadening caused by micro gas motions will affect the appearance of red profiles. Different from those of bipolar outflows, emission lines from clouds under EECC dynamics will grossly show circular spatial symmetry, and the flow speed is typically smaller (e.g.  $\sim 0.1 - 1 \text{ km s}^{-1}$ ). By fitting spectral emission line profiles of certain dynamic models with observed emission lines from star-forming clouds, it is possible to resolve the dynamic structures of these molecular clouds. These processes will also give rise to more physical parameters of forming protostars and its cloud environment.

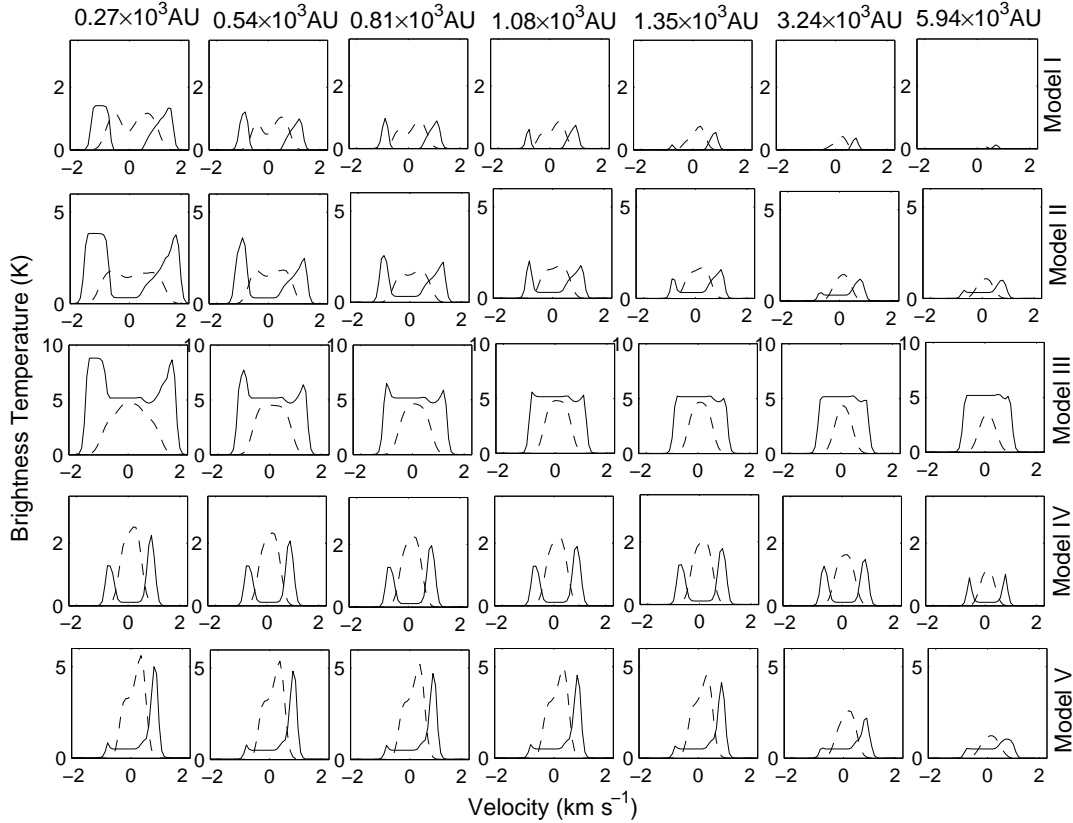


**Figure 6.** Model calculations for spectral line profiles of CO(2–1) at 230.54 GHz (solid curves) and C<sup>18</sup>O(1–0) at 109.78 GHz (dashed curves) from individual pixels of spatially resolved emission lines for five EECC dynamic Models I–V. The ordinate is the brightness temperature in Kelvin and the abscissa is the projected velocity component in the local standard of rest (LSR) in unit of km s<sup>−1</sup>. Rows from top to bottom show molecular line profiles for different dynamic Models I–V, respectively. Panels from left to right present LOS with different impact parameter  $b$ , which are not uniformly chosen such that spatial transitions between blue profiles and red profiles are clearly identified for Models I, II and III. The intrinsic line broadening is  $\Delta u = 0.5$  km s<sup>−1</sup>.

## ACKNOWLEDGMENTS

This research was supported in part by Tsinghua Centre for Astrophysics (THCA), by the National Natural Science Foundation of China (NSFC) grants 10373009 and 10533020 at Tsinghua University, and by the Yangtze Endowment and the SRFDP 20050003088 and 200800030071 at Tsinghua University. The hospitality of Institut für Theoretische Physik und Astrophysik der Christian-Albrechts-Universität Kiel Germany and of International Center for Relativistic Astrophysics Network (ICRANet) Pescara, Italy is gratefully acknowledged. YG thanks Y. Wu for assistance in running the RATRAN code.

## REFERENCES

- Adams F. C., 1991, *ApJ*, 382, 544  
 Adelson L. M., Leung C. M., 1988, *MNRAS*, 235, 349  
 Aguti E. D., Lada C. J., Bergin E. A., Alves J. F., Birkinshaw M., 2007, *ApJ*, 665, 457  
 Arons J., Max C. E., 1975, *ApJ*, 196, L77  
 Belloche A., André P., Despois D., Blinder S., 2002, *A&A*, 393, 927  
 Bernes C., 1979, *A&A*, 73, 67  
 Bian F. Y., Lou Y.-Q., 2005, *MNRAS*, 363, 1315  
 Carolan P. B., Redman M. P., Keto E., Rawlings J. M. C., 2008, *MNRAS*, 383, 705  
 Di Francesco J., Myers P. C., Wilner D. J., Ohashi N., Mardones D., 2001, *ApJ*, 562, 770  
 Evans N. J. II, 2003, in *Proc. of Conf., Chemistry as a Diagnostic of Star Formation*, eds. Curry C. L., Fich M., NRC Research Press, p.157  
 Evans N. J. II, Dunham M. M., Jørgensen J. K., Enoch M. L., Merín B., van Dishoeck E., Alcalá J. M., Myers P. C., et al., 2009, *ApJS*, 181, 321  
 Fiege J. D., Henriksen R. N., 1996a, *MNRAS*, 281, 1038  
 Fiege J. D., Henriksen R. N., 1996b, *MNRAS*, 281, 1055  
 Fuller G. A., Williams S. J., Sridharan T. K., 2005, *A&A*, 424, 949  
 Gao Y., Lou Y.-Q., Wu K., 2009, *MNRAS*, in press (2009arXiv0908.0978G)  
 Hammersley J. M., Handscomb D. C., 1964, *Monte Carlo Methods*, Methuen Press, London  
 Harvey D. W. A., Wilner D. J., Myers P. C., 2003, *ApJ*, 583, 809  
 Hennebelle P., Chabrier G., 2008, *ApJ*, 684, 395

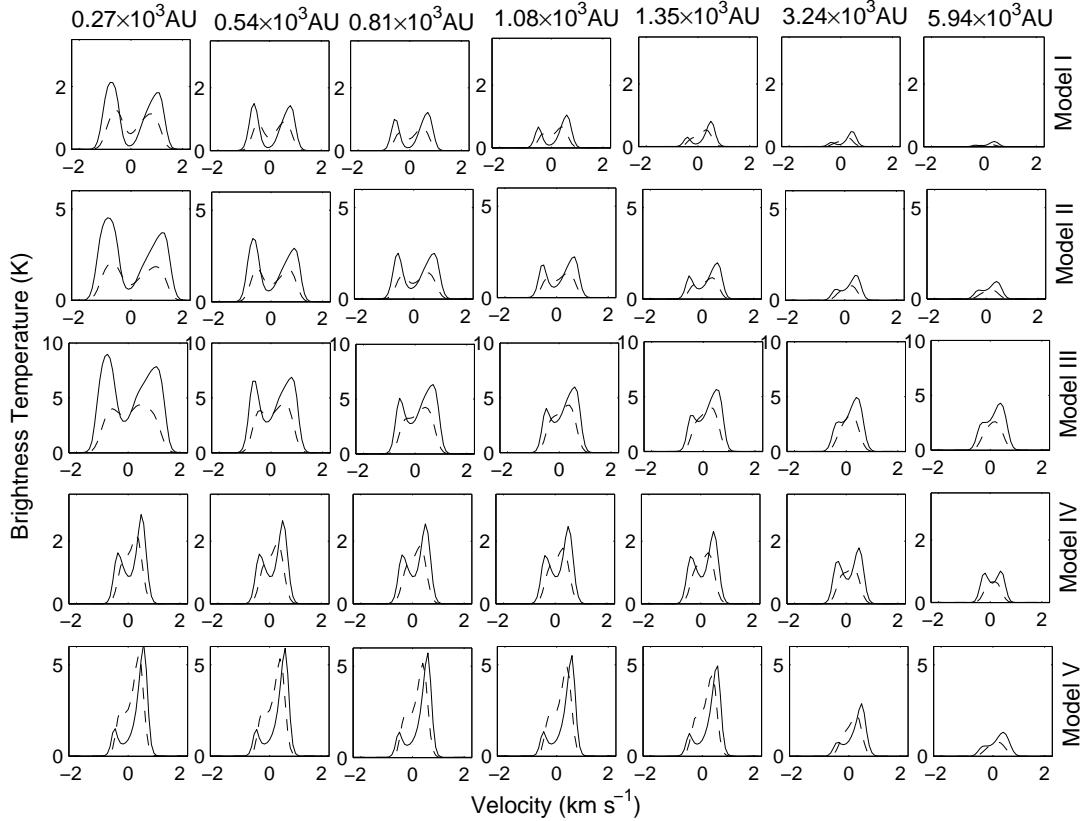


**Figure 7.** Model calculations of spectral molecular line profiles of CS(2 – 1) at 97.98 GHz (solid curves) and N<sub>2</sub>H<sup>+</sup>(1 – 0) at 93.13 GHz (dashed curves) from individual pixels of spatially resolved emission lines for five EECC dynamic Models I–V. The ordinate is the brightness temperature in Kelvin and the abscissa is the projected velocity component in the local standard of rest (LSR) in unit of km s<sup>–1</sup>. Rows from top to bottom show molecular line profiles for different dynamic Models I–V, respectively. Panels from left to right present LOS with different impact parameter  $b$ , which are not uniformly chosen such that transitions between blue profiles and red profiles are clearly identified for Models I, II and III. The intrinsic line broadening is  $\Delta u = 0.5$  km s<sup>–1</sup>.

- Hogerheijde M. R., Sandell G., 2000, *ApJ*, 534, 880  
 Hu R. Y., Lou Y.-Q., 2008, *MNRAS*, 390, 1619  
 Jørgensen J. K., et al., 2007, *ApJ*, 659, 479  
 Kenyon S. J., Hartmann L. W., Strom K. M., Strom S. E., 1990, *AJ*, 99, 869  
 Keto E., Broderick A. E., Lada C. J., Narayan R., 2006, *ApJ*, 652, 1366  
 Lada C. J., Bergin E. A., Alves J. F., Huard T. L., 2003, *ApJ*, 586, 286  
 Larson R. B., 1981, *MNRAS*, 194, 809  
 Lee J.-E., Kim J., 2009, *ApJ*, 699, L108  
 Lou Y.-Q., Rosner R., 1986, *ApJ*, 309, 874  
 Lou Y.-Q., Shen Y., 2004, *MNRAS*, 348, 717  
 Lou Y.-Q., Gao Y., 2006, *MNRAS*, 373, 1610  
 Lou Y.-Q., Hu R. Y., 2009, *New Astronomy*, in press (2009arXiv0905.3490L)  
 MacLow M.-M., 1999, *ApJ*, 524, 169  
 Mardones D., Myers P. C., Tafalla M., Wilner D. J., 1997, *ApJ*, 489, 719  
 Matthews B. C., Hogerheijde M. R., Jørgensen J. K., Bergin E. A., 2006, *ApJ*, 652, 1374  
 Matzner C. D., McKee C. F., 1999, *ApJ*, 526, L109  
 Matzner C. D., McKee C. F., 2000, *ApJ*, 545, 364  
 McKee C. F., Ostriker E. C., 2007, *ARA&A*, 45, 565  
 Moraghan A., Smith M. D., Rosen A., 2008, *MNRAS*, 386, 2091  
 Moriarty-Schieven G. H., Butner H. M., Wannier P. G., 1995, *ApJ*, 445, L55  
 Myers P. C., 2005, *ApJ*, 623, 280  
 Myers P. C., 2008, *ApJ*, 687, 340  
 Nakano T., Hasegawa T., Norman C., 1995, *ApJ*, 450, 183  
 Ossenkopf V., 2002, *A&A*, 391, 295  
 Ostriker E. C., *ApJ*, 486, 291  
 Park Y.-S., Yun H. S., Hong S. S., Lee H. M., 1992, *JKAS*, 65, 25  
 Park Y.-S., Panis J.-F., Ohashi N., Choi M., Minh Y. C., 2000, *ApJ*, 542, 344  
 Park Y.-S., Lee C. W., Myers P. C., 2004, *ApJS*, 152, 81  
 Rawlings J. M. C., Yates J. A., 2001, *MNRAS*, 326, 1423  
 Redman M. P., Keto E., Rawlings J. M. C., Williams D. A., 2004, *MNRAS*, 352, 1365  
 Redman M. P., Keto E., Rawlings J. M. C., 2006, *MNRAS*, 370, L1  
 Saito M., Sunada K., Kawabe R., Kitamura Y., Hirano N., 1999, *ApJ*, 518, 334  
 Schöier F. L., van der Tak F. F. S., van Dishoeck E. F.,

- Black J. H., 2005, *A&A* 432, 369
- Shang H., Allen A., Li Z.-Y., Liu C.-F., Chou M.-Y., Anderson J., 2006, *ApJ*, 649, 845
- Shen Y., Lou Y.-Q., 2004, *ApJ*, 611, L117
- Shirley Y. L., Evans N. J. E., Rawlings J. M. C., Gregersen E. M., 2000, *ApJS*, 131, 249
- Shreider Yu. A., ed. 1966, *The Monte Carlo Method*, Pergamon Press, Oxford
- Shu F. H., 1977, *ApJ*, 214, 488
- Shu F. H., Adams F. C., Lizano S., 1987, *ARA&A*, 25, 23
- Shu F. H., Ruden S. P., Lada C. J., Lizano S., 1991, *ApJ*, 370, L31
- Shu F., Najita J., Ostriker E., Wilkin F., Ruden S., Lizano S., 1994, *ApJ*, 429, 781
- Su Y.-N., Liu S.-Y., Chen H.-R., Zhang Q., Cesaroni R., 2007, *ApJ*, 671, 571
- Tafalla M., Myers P. C., Mardones D., Caselli P., Bachiller R., Benson P. J., 1998, *ApJ*, 504, 900
- Tafalla M., Mardones D., Myers P. C., Bachiller R., 2000, *A&A*, 359, 967
- Tafalla M., Santiago J., Myers P. C., Caselli P., Walmsley C. M., Crapsi A., 2006, *A&A*, 455, 577
- Thompson M. A., White G. J., 2004, *A&A*, 419, 599
- Tsamis Y. G., Rawlings J. M. C., Yates J. A., Viti S., 2008, *MNRAS*, 388, 898
- van der Tak F. F. S., Caselli P., Ceccarelli C., 2005, *A&A*, 439, 195
- Van Zadelhoff G.-J., et al., 2002, *A&A*, 395, 373
- Velusamy T., Peng R., Li D., Goldsmith P. F., Langer W. D., 2008, *ApJ*, 688, L87
- Wang W.-G., Lou Y.-Q., 2008, *Ap&SS*, 315, 135
- Ward-Thompson D., Buckley H. D., 2001, *MNRAS*, 327, 955
- Wilner D. J., Myers P. C., Mardone S., Tafalla M., 2000, *ApJ*, 544, L69
- Wu Y., Zhang Q., Chen H., Yang C., Wei Y., Ho P. T. P., 2005, *AJ*, 129, 330
- Yu C., Lou Y.-Q., 2005, *MNRAS*, 364, 1168
- Yu C., Lou Y.-Q., Bian F. Y., Wu Y. 2006, *MNRAS*, 370, 121
- Zhou S., Evans N. J. II, Kömpe C., Walmsley C. M., 1993, *ApJ*, 404, 232
- Zhou S., 1995, *ApJ*, 442, 685
- Zweibel E. G., McKee C. F., 1995, *ApJ*, 439, 779